LLNL-JRNL-838442

ATHENA: A Unique Radiation Environment Platform at the National Ignition Facility

N. J. Quartemont, G. Peterson, C. Moran, A. Samin, B. Wang, C. B. Yeamans, B. Woodworth, D. Holland, J. Petrosky, J. E. Bevins

August 3, 2022

Nuclear Instruments and Methods in Physics Research Section A

LLNL-JRNL-838442

Nuclear Inst. and Methods in Physics Research, A

ATHENA: A unique radiation environment platform at the National Ignition Facility

Nicholas J. Quartemont [a,*], George Peterson [a], Colton Moran [a], Adib Samin [a], Buguo Wang [a,b], Charles Yeamans [c], Brandon Woodworth [c], Darren Holland [a], James C. Petrosky [a], James E. Bevins [a]

[a] *Department of Engineering Physics, Air Force Institute of Technology, WPAFB, OH 45433, USA*
[b] *Department of Physics, Wright State University, Dayton, OH 45435, USA*
[c] *Lawrence Livermore National Laboratory, Livermore, CA 94550, USA*

ARTICLE INFO

Keywords:
Short-pulse neutron source
Neutron energy tuning
Radiation effects experiment
Neutron spectrum unfolding

ABSTRACT

This paper describes the ATHENA platform, an energy tuning assembly, which was developed to spectrally shape the National Ignition Facility (NIF) deuterium–tritium fusion neutron source to a thermonuclear (fusion) plus prompt fission neutron spectrum with a capability to act as a short-pulse neutron source. This unique, otherwise inaccessible radiation environment complements existing experimental facilities and capabilities. The flexible ATHENA irradiation positions were modeled using an ensemble of Monte Carlo simulations with stochastic sampling of the nuclear cross-sections to characterize the radiation environments and uncertainty for the platform. Validation of the internal neutron spectrum produced from fielding ATHENA at NIF occurred through neutron flux unfolding with 20 measured activation products. The STAYSL unfolded neutron flux resulted in a reduced χ^2 value of 1.4 with a larger contribution from ^{46}Ti(n,2n) reaction channel. The total ionizing dose was measured to be 515 ± 7.9% rad(TLD-400), whereas the modeled values indicated a lower value of 290 ± 4.6% rad(TLD-400). The NIF experiment demonstrated that ATHENA is capable of producing a thermonuclear and prompt fission neutron spectrum with a 50 nanosecond pulse width and a 1-MeV equivalent neutron fluence of 3.6×10^{12} $\frac{n}{cm^2}$ with strong radial uniformity over the sample volume. Example case studies of ATHENA for integral experiments and microelectronic device responses are also presented.

1. Introduction

Customizable neutron source development through energy tuning assemblies (ETAs) provides a capability to explore inaccessible radiation environments by spectrally modifying existing neutron facilities [1–4]. These unique environments can have key applications in nuclear sciences and engineering such as nuclear data and validation experiments to benchmark integral experiment models [5,6]. Additionally, these customizable radiation sources can be used to further radiation effects on electronics testing to provide a spectrally accurate source term on relevant timescales. Current and past sources for neutron testing have limitations on the neutron energy spectrum, timing, and γ-ray contributions to the radiation environment, a long standing challenge for the community [7]. Fast burst reactors such as the dismantled Sandia Pulse Reactor-III or at White Sands Missile Range have proved to be the gold standard for prompt fission spectrum neutron irradiation with 5×10^{14} 1-MeV(Si) $\frac{\mathrm{n}}{\mathrm{cm}^2}$ over longer nuclear-weapon-relevant time scales [8,9]. However, due to concerns over special nuclear material and increased development, other types of facilities have seen an increase in utilization as neutron sources for national security experiments.

Facilities such as the National Ignition Facility (NIF) can provide a clean source of 14.1 MeV neutrons from deuterium–tritium (D-T) fusion reactions above 10^{13} 1-MeV(Si) $\frac{\mathrm{n}}{\mathrm{cm}^2}$ with little γ-ray contamination [10]. The 1-MeV(Si) fluence, a common equivalency used for radiation effects testing, is represented as a weighted integration of neutron fluence with the weighting function based on the equivalency of energy-dependent displacement damage as outlined in ASTM 19–722 [11]. Spallation neutron sources like the Los Alamos Neutron Science Center (LANSCE) can provide 2×10^{12} 1-MeV(Si) $\frac{\mathrm{n}}{\mathrm{cm}^2}$ over a short 100+ ns timescale with a low γ-ray environment, but the neutron spectrum is spread over a much larger and higher range of neutron energies [12]. Ion beam sources can produce near 5×10^{13} 1-MeV(Si) $\frac{\mathrm{n}}{\mathrm{cm}^2}$ over a moderate 40 μs timescale, but they also require an equivalence factor between ion and neutron damage [12,13]. Nuclear reactors such as the Annular Core Research Reactors can produce in excess of 10^{15} 1-MeV(Si) $\frac{\mathrm{n}}{\mathrm{cm}^2}$ over a longer 6 ms timescale in pulsed

* Corresponding author.
E-mail address: nicholas.quartemont@afit.edu (N.J. Quartemont).

mode; however, they include a larger ionizing dose with a thermalized neutron spectrum [14].

The ATHENA platform was designed as an ETA to produce a thermonuclear and prompt fission spectrum (TN+PFNS) through spectral modification of the NIF D-T neutron source. The payload is a second-generation design to the precursor ETA proof-of-concept platform. The original ETA design, fielded at the NIF to measure highly enriched uranium fission products, produced a prompt TN+PFNS and validated the modeling methodology [1]. Improvements to the ATHENA platform from the original ETA include an optimized physical geometry that allows for a 6 cm standoff range to the NIF source (compared to the previous 15 cm), improved efficiency (higher fluence at the target position), and reduced weight allowing more flexible implementation. Additionally, the experimental irradiation volume has been expanded to a 7 cm diameter, 8 cm high cylindrical irradiation configuration with an external primarily D-T irradiation position to allow for multiple, larger experiments to be conducted on one platform. The enhanced capability on ATHENA can provide up to 3.6×10^{12} 1-MeV(Si) $\frac{\text{n}}{\text{cm}^2}$ for a 10^{16} source neutron D-T shot yield on a 50 ns timescale.

This paper is organized as follows. Section 2 describes the optimization and design of the ATHENA payload and supporting diagnostic equipment available. Section 3 outlines the radiation environment, modeling methodology, and provides validation of the ATHENA resulting source environment during a NIF shot. Section 4 provides use-cases for the ATHENA platform to include integral nuclear data measurements and microelectronic device responses under the unique ATHENA environment. Finally, Section 5 summarizes the uncertainty quantification techniques and provides a path forward for future work.

2. Experimental setup

This section describes the optimization of the internal ATHENA neutron spectrum, mechanical hardware, and supporting diagnostics for experiments. The experimental concept allows for an internal spectrally-shaped neutron spectrum and optional externally-mounted irradiation position, which adds to the experimental efficiency to take multiple, equivalent 1-MeV(Si) fluence measurements on the ATHENA platform. The internal radiation environment cavity utilizes a removable plug to add the larger irradiation volume for the spectrally-modified neutron source, and the internal neutron environment is characterized with an drawer containing activation foils. The ATHENA validation experiment, discussed further in Section 3.2.1, is shown in Fig. 1 for an experimental validation of the internal radiation environment created 9 cm from the NIF target chamber center (TCC) during NIF shot N201128-001. A repository containing the ATHENA design, materials, and models used in this work is available [15].

2.1. Design optimization

ATHENA was designed with the ETA software, Coeus V1.0 [3], leveraging the Gnowee metaheuristic optimization algorithm [16]. Coeus functions as a wrapper to call MCNP [17] neutron transport simulations for candidate ETA designs provided by Gnoewee. Each candidate ETA design was defined with an outer design envelope containing cylinders and cones that are filled with materials to spectrally modify the NIF point neutron source into a target neutron spectrum. The population-based Gnowee algorithm optimized the ATHENA geometry and materials based on a set of objectives and constraints with heuristic search strategies described in previous work [16].

The objective function was defined as a desired TN+PFNS relevant to induced neutron environments within the ATHENA sample drawer shown in Fig. 1. A combination of 85% volume distributed fission spectrum neutrons and 15% D-T point source neutrons were transported within a 10.2 cm beryllium reflected highly enriched uranium (HEU) critical assembly [18]. The volume-averaged neutron flux within the critical assembly was used for the objective TN+PFNS.

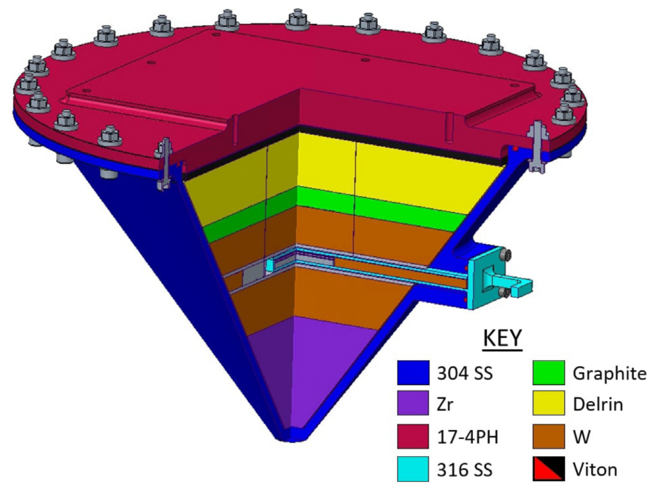

Fig. 1. (Color online) N201129-001 NIF shot ATHENA platform. The ATHENA neutron spectral-shaping package was mounted on diagnostic instrument mount 90–348 and the D-T capsule target was at the end of the target positioner, 9 cm from the base of ATHENA.

Two general constraints were applied to the ATHENA optimization. First, candidate designs required a minimum threshold neutron fluence of 3×10^{12} n-cm^{-2} in the drawer sample cavity. Second, there were several NIF facility constraints including the weight and ATHENA geometry envelope. The weight was constrained to a maximum of 120 kg; the fluence and weight constraint were implemented by discarding a candidate design if the constraint was not met. The design was set 6 cm from the D-T source at target chamber center (TCC) based on the facility's laser exclusion zones, and the design was constrained to a maximum diameter of 30 cm based on the available ports to field the platform.

The Coeus generated ATHENA design with engineering modifications and additional manufacturing detail is shown in Fig. 1. Engineering modifications were made to the design to remove non-contributing components and increase the thermal neutron population with the addition of the back polyoxymethylene (Delrin) thermoplastic layer, leading to the final ATHENA hardware discussed in Section 2.2. Isotopic concentration uncertainty was limited by utilizing materials with 99 to 99.95% purity. The front zirconium and tungsten layers provide the primary inelastic and (n,2n) reaction channels as a source term for the PFNS. The back graphite carbon and Delrin, with a density of 1.40 g-cm^{-3}, layers increase the low energy neutron population in the assembly while also acting as a reflector to increase the overall fluence in the experimental cavity.

The available irradiation positions on ATHENA are highlighted in Fig. 2. The spectrally shaped internal radiation environment includes a drawer sample region and removable plug cylindrical volume. The external environment, with minimal spectral shaping, is positioned to face the target chamber center (TCC), which is the source location of the D-T fusion neutrons.

2.2. Mechanical hardware

The internal ATHENA cavity was created with a removable plug past the primary spectral modification material, allowing for an expanded device irradiation volume and room for connecting electronics. A rapidly-extractable sample drawer is positioned containing neutron activation foils and thermoluminescent dosimeters (TLDs) to measure the neutron and ionizing radiation environment, respectively. The internal cavity region is accessible post-shot through a port in the back of the platform.

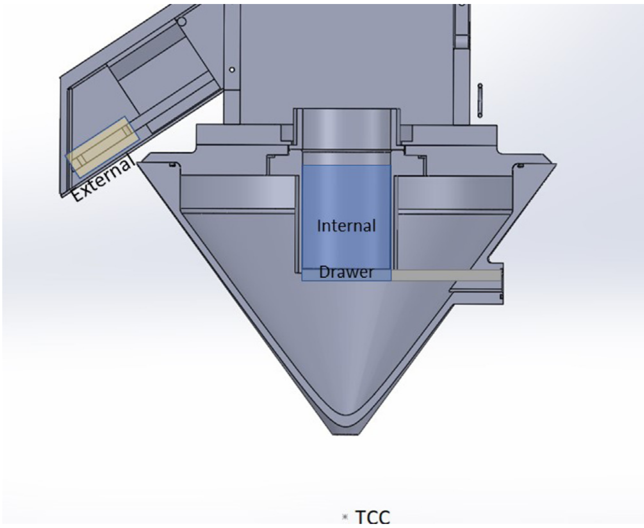

Fig. 2. (Color online) ATHENA platform with internal drawer, internal cavity, and external arm irradiation positions.

The external region contains a removable sled that is also accessible through the port, and a second diagnostic set of activation foils and TLDs can be positioned here. Retrieval times are dependent on facility safety constraints based on the achieved source yield for a shot; samples for a $1{\times}10^{16}$ neutron yield can typically be recovered for analysis within a couple of hours.

The ATHENA platform was designed with re-usable internal components, but they can be replaced for quasi-customizable environments within the assembly's defined outer envelope. Additionally, replacing spectral modification material layers could directly test specific isotopic reaction contributions to the integral result in validation experiments.

2.3. Diagnostics

Radiation environments can be characterized with both passive and active diagnostics to benchmark models and inform on experimental conditions. Two passive diagnostics utilized on the ATHENA platform are activation foils and TLDs, to measure the integral neutron and ionizing radiation environments, respectively. Active diagnostics can include radiation measurement devices such as CVD diamond detectors or powered semiconductor component devices.

The neutron diagnostic activation foils fielded for the ATHENA environment validation experiment are summarized in Table 1. Each of the reactions are included in the International Reactor Dosimetry and Fusion File (IRDFF) nuclear data library and have half-lives allowing for spectroscopy from several hours to days post-experiment [19]. The materials and reactions were chosen to cover the broad energy range of the modified neutron spectrum, while maintaining an optically "thin" foil stack. The measured resulting activation products were used to unfold the experimental neutron energy spectrum.

The internal drawer of ATHENA also has positions for eight $3.2 \times 3.2 \times 0.89$ mm Thermo Fisher Scientific TLD-400 and/or TLD-100 chips for a passive integral ionizing dose measurement. Similar to the activation foils, the same capability to field eight TLD chips also exists for the external position. For the ATHENA-I experiment four TLD-400 chips were fielded.

Active diagnostics within the NIF facility are also important diagnostics for modeling the radiation environment for these types of experiments. The D-T shot yield to scale modeling results can be determined with neutron activation spectrometers relying on ^{90}Zr(n,2n) to determine the primary D-T [34]. The emission neutron energy spectrum, total yield, and the plasma ion temperature can be measured with neutron time-of-flight (nTOF) scintillators available within the chamber [35]. Additionally the source emission angular distribution, which is generally considered as a isotropic point source, can be assessed with pinhole neutron topography measurements [36].

3. Environment characterization

The ATHENA radiation environment was characterized with Monte Carlo radiation transport codes, and the internal neutron and γ-ray fields were experimentally validated during an integral measurement experiment. MCNP6 was used to model the continuous energy radiation transport environment, and the SCALE 6.3 Beta 14 MAVRIC and Sampler modules were used to assess the effect of nuclear data covariance on the neutron transport throughout the geometry [17,37]. The internal ATHENA irradiation position in the drawer was validated using temporal and energy integrated activation foils to unfold the neutron fluence spectrum. Additionally, TLD-400s (CaF_2:Mn) were fielded to provide an integrated ionizing dose measurement inside the sample cavity.

3.1. Simulation methodology

The modeling and nuclear data covariance methodology have been introduced in previous work on the original ETA [1,2]. The as-fielded ATHENA platform and the surrounding NIF equipment were modeled in MCNP6 to obtain the continuous energy radiation environments in the sample irradiation positions using a full-scale NIF model. SCALE 6.3 Beta 14 MAVRIC-shift with Sampler was used to propagate nuclear data covariance in the neutron transport model to bound the neutron spectrum for unfolding with STAYSL [17,37]. MAVRIC simulations were then used in a 1597 energy group structure with the SCALE Sampler module to assess the effect of nuclear data covariance through stochastic sampling of the neutron energy group ENDF-B/VIII.0 nuclear data library [38].

The IRDFF nuclear data library was used for activation foil reaction cross-sections and covariance matrices [19,39]. The IRDFF v.1.05 library was used here due to compatibility with the currently obtained release of STAYSL; however, minimal changes for the chosen reactions have been updated in the IRDFF-II library. Updated reactions include ^{197}Au(n, (g) ^{198}Au. Additionally, the updated IRDFF-II library includes natural titanium reaction products that have multiple production pathways. Not using the IRDFF-II library resulted in negligible impact to the experiment analysis, but not having the natural target reaction product measurements required splitting the contributions for Sc reaction products based on the modeled reactions.

3.2. Neutron environment

The polar-direct-drive exploding pusher (PDXP) neutron source fielded for the ATHENA experiment, one of the available targets at NIF, utilizes a gas filled D-T mixture without a hohlraum [40]. Capsules typically have low mass which significantly reduces down-scattering within the target area resulting in a nearly pure D-T fusion neutron spectrum [41]. The laser driven targets can achieve neutron yields on the order 10^{16} with an ion-temperature of approximately 10 keV and a emission time near 300 ps.

The ATHENA shot source utilized a 50/50 D-T mix capsule with a 1.96 mg mass, 23 μm thick, and 4.95 mm outer diameter. The NIF laser system delivered 1.58 MJ of laser energy yielding $6.35 \pm 0.24 \times 10^{15}$ neutrons over 500 ps [42]. The NIF source was modeled based on the nTOF signal located at position 116–316, the most closely positioned detector to the ATHENA-I experiment position at 90–348. The neutron spectrum in the room does have anisotropies, so using the closest diagnostic is important to capture some of the energy dependency as a function of position in the chamber. The experimental neutron spectrum, depicted in Fig. 3, was calculated based on the nTOF signal using a linear least squares fit to the convolution of the neutron spectrum with the nTOF instrument response function and detection efficiency [35].

Table 1
Neutron spectrum unfolding activation foils and reactions utilized for ATHENA irradiation positions. The foils are listed in order with Au-1 closest to TCC.

Foil (thickness)	Mass [g]	Reaction	Threshold [MeV] (@ 10 mb)	Primary radiation [keV] (intensity)	$t_{1/2}$	Decay data
Au-1 (0.05 mm)	1.883	^{197}Au(n,2n)^{196}Au^{g+m1}	8.1 (8.3)	355.7 (0.87)	6.17 days	[20]
		^{197}Au(n,g)^{198}Au	Thermal	411.8 (0.9562)	2.69 days	[21]
Ni (0.23 mm)	4.073	^{58}Ni(n,2n)^{57}Ni	12.4 (13.3)	1378 (0.817)	35.6 h	[22]
		^{58}Ni(n,p)^{58}Co^{g+m1}	0 (1.3)	810.8 (0.9945)	70.86 days	[23]
In (0.27 mm)	3.665	^{113}In(n,n′)^{113}In^{m1}	0.4 (0.7)	391.7 (0.6494)	99.5 min	[24]
		^{115}In(n,n′)^{115}In^{m1}	0.336 (0.597)	336.24 (0.459)	4.49 h	[25]
		^{115}In(n,g)^{116}In^{m1}	Thermal	1293.56 (0.848)	54.29 min	[26]
Al (0.73 mm)	3.793	^{27}Al(n,a)^{24}Na	3.25 (6.7)	1368.63 (0.9999)	15 h	[27]
Ti (0.25 mm)	2.112	^{46}Ti (n,2n) ^{45}Ti	13.5 (14)	511.0 (1.696)	184.8 min	[28]
		^{nat}Ti(n,x)^{46}Sc	2.1 (6)	1120.5 (0.9999)	83.79 days	[29]
		^{nat}Ti(n,x)^{47}Sc	0.8 (10.5)	159.38 (0.683)	3.3492 days	[30]
		^{nat}Ti(n,x)^{48}Sc	3.3 (7.5)	1312.1 (1.001)	43.67 h	[31]
W (0.12 mm)	4.304	^{186}W(n,g)^{187}W	Thermal	685.51 (0.332)	24 h	[32]
Zr (0.27 mm)	3.083	^{90}Zr(n,2n)^{89}Zr	12.1 (12.1)	909.2 (0.9904)	78.41 h	[33]
Mg (0.09)	0.318	^{24}Mg(n,p)^{24}Na	4.9 (6.4)	1368.63 (0.9999)	15 h	[27]
Au-2 (0.05 mm)	1.884	^{197}Au(n,2n)^{196}Au^{g+m1}	8.1 (8.3)	355.7 (0.87)	6.17 days	[20]
		^{197}Au(n,g)^{198}Au	Thermal	411.8 (0.9562)	2.69 days	[21]

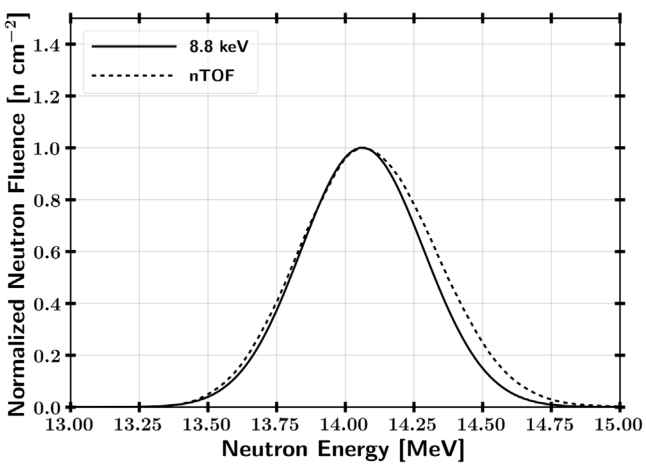

Fig. 3. NIF shot N201128-001 calculated neutron spectrum on nTOF 116-316 in comparison to a theoretical 8.8 keV ion-temperature model [43].

The measured ion-temperature plasma was 8.8 keV, and the experimental source spectrum was generally in agreement with a theoretical plasma distribution with a 8.8 keV ion-temperature plasma based on [44]. However, there was an increase in the high energy neutron population due to upscattering reactions within the source itself. Also noteworthy is that the increase in high energy neutrons was not seen on nTOF 90-174, further indicating the angular asymmetry of the PDXP source. Time dependence in the neutron source was neglected in the Monte Carlo simulations due to short emissions relative to neutron transport within ATHENA [45].

Fig. 4 highlights the simulated induced neutron environments, where the plug is removed. The drawer and center cavity results indicate that the internal environments produced during a NIF shot provide a nearly uniform TN+PFNS, where the thermal population of neutrons increases farther back in the cavity. The external neutron spectrum is primarily uncollided source neutrons with a scattered PFNS contribution from the central ATHENA platform itself.

The simulated neutron fluence covariance results for the internal drawer neutron spectrum from 300 samples in Sampler running MAVRIC with the 1597-group structure were characterized with statistical bootstrapping to determine a 1-σ uncertainty in the fluence distribution mapped to the 129-group STAYSL structure. The Sampler neutron transport uncertainty and flux correlation matrix for the internal cavity spectrum are shown in Fig. 5. The resultant covariance matrix was used in STAYSL to bound the neutron flux distribution.

At energies approaching the source D-T neutrons, the uncertainty is approximately 1%–2%. Near 1 MeV, the uncertainty was lower than the source region because multiple reactions paths over few interactions are able to populate this region. At lower energies, the uncertainty grows to nearly 100% due to the large amount of scattering reactions required to reach these energies. Additionally, the radiative capture resonances in the tungsten layer cause large uncertainty near 10 eV, where even small uncertainties can compound over the tens to hundreds of mean free paths required to pass into the sample drawer. Note, the ENDF-B/VIII.0 library, which was the source of the nuclear data covariance, did not include W(n,2n) reaction uncertainty. Thus, the results underestimate the uncertainty and correlation between the TN and PFNS components.

3.2.1. ATHENA-I validation

ATHENA was fielded at 9 cm from TCC on diagnostic instrument manipulator (DIM) 90-348. This position is 3 cm farther from the minimum distance that the platform can be placed due to an external flange obstructing the laser paths, and the design has been updated for future experiments to remove this piece, as shown when comparing Figs. 1 and 2. The activation analysis performed was similar to the method outlined in previous research on the ETA experiment [1]. Post-shot activation analysis was performed on the activation foils with γ-ray spectrometry using three high purity germanium (HPGe) and multi-channel analyzer systems in the Lawrence Livermore National Laboratory counting facility [46]. PeakEasy 4.99 was used for peak fitting with energy-dependent counts and efficiency as calculated with GAMANAL [47,48]. Standard calibration sources were used to determine each HPGe detector's efficiency as a function of sample position, energy, and detector geometry.

Each foil was counted until approximately 10,000 counts were detected in high-intensity photopeaks, and the activity measurements were decay corrected to the reaction product atoms immediately after irradiation. A variance-based weighted average was taken for each decay γ-ray associated with a product nuclei for each measurement of that decay mode [49]. The final weighted average of each γ-ray decay mode measurement was then completed to determine the amount of each product. Radioactive decay uncertainties were added in quadrature after accounting for the statistical error and a 2% detection systematic error [49].

The measured foil activation products were used with the modeled MCNP6 neutron fluence and SCALE Sampler neutron fluence covariance to unfold the neutron spectrum using STAYSL with the IRDFF v.1.05 129-energy group structure. STAYSL determines the incident neutron flux using a generalized least-squares spectral adjustment

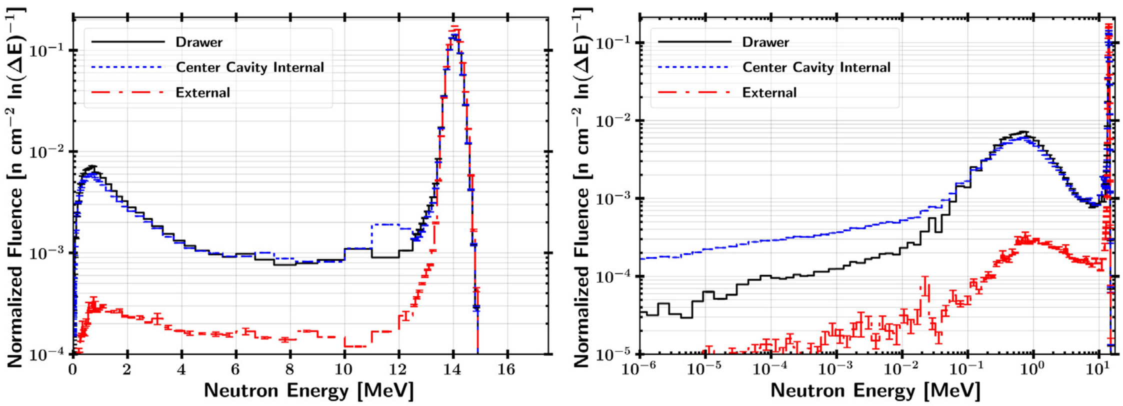

(a) Linear Energy Scale

(b) Logarithmic Energy Scale

Fig. 4. (Color online) ATHENA internal drawer, center cavity, and external neutron spectra highlighting the spectrally shaped neutron and external D-T neutron environments achievable for testing.

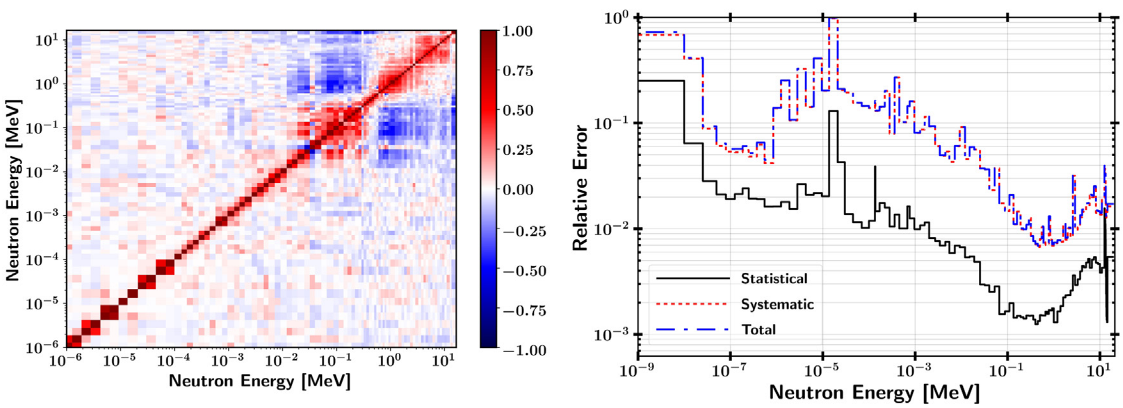

(a) Correlation matrix

(b) Relative Uncertainty

Fig. 5. (Color online) Neutron fluence covariance parameters for internal ATHENA sample cavity showing the (a) correlation matrix and (b) relative statistical and systematic uncertainty as a function of energy. The covariance matrix formed from the correlation matrix and relative uncertainty was used to bound the neutron spectrum unfolding in STAYSL.

based on a χ^2 comparison of the measured activation products and the activities calculated from an adjusted flux [50]. Additionally, STAYSL requires an initial guess spectrum as the activities produced for the foils are often degenerate with multiple possible creation environments. However, the initial spectrum allows for a physics and modeling-based result to guide the overall result.

The neutron irradiation time is much shorter than the half-lives of the product isotopes, so the effects of saturation and decay during irradiation are negligible. Reaction channels with multiple feeding paths were split based on the modeled contributions. Activation foil self-shielding correction factors were created based on the MCNP6 model [1].

The experimental results for 20 activation products used in STAYSL are summarized in Table 2. For each reaction, the saturation activity, σ-ϕ, and associated measurement error are given. The saturation activity utilized the short-pulse approximation, where the value reflects the equivalent total number of atoms produced divided by the total target atoms. STAYSL χ^2 contributions include the difference from the measurement to the optimized modeled solution with covariance information from the measurement, neutron fluence, and activation cross-sections. Additionally, the percent error relative to the measurement and 5 to 95% activation range where the activation product informs the unfolding procedure are provided.

The STAYSL unfolded neutron spectrum for the internal drawer of ATHENA is shown in Fig. 6. The STAYSL χ^2 per degree of freedom was 1.38, indicating general agreement with the modeled neutron flux and covariance. The ^{46}Ti(n,2n)^{45}Ti was the least well performing reaction, where the other high energy reaction products aside from ^{45}Ti agreed with the model. Since the NIF neutron source is not isotropic, and the nTOF detectors are not perfectly aligned with the experimental platforms, it is possible that the neutron spectrum at the ATHENA platform on 90–348 was different than on 116–316. Additionally, the missing covariance information for W(n,2n) reactions underestimated the uncertainty, thereby leading to an overly constrained neutron spectrum. This would require evaluated data available in SCALE to remedy.

3.2.2. Neutron displacement damage

Neutron displacement damage and related effects are also an important characteristic of the ATHENA environments. Engineering-level neutron environmental metrics have been historically used to define a neutron spectrum and fluence in terms of mono-energetic neutrons defined in ASTM E722–19 [11,51]. These metrics are applicable when the majority of displacement damage is from neutrons above 10 keV and assumes charged particle equilibrium. The displacement damage function, $F_{D,material}$, can be used to relate the 1-MeV neutron equivalent fluence to an observable effect, such as the gain degradation of a silicon-based transistor. The 1-MeV neutron equivalent fluence for elemental silicon is given by,

$$\Phi_{eq,1\text{-MeV,Si}} = \frac{\int_0^\infty \Phi(E) F_{D,\mathrm{Si}}(E) dE}{F_{D,1\text{-MeV,Si}}}, \tag{1}$$

Table 2
ATHENA validation experiment reaction channels for STAYSL unfolding with measured value and error. The χ^2 contribution to the total and percent error from the model are also given, where negative percent errors represent that a activation product was under-produced at the experiment. The 5 to 95% activation energy range corresponds to the energy interval where the activation products inform the unfold.

Measured reaction	Measurement [σ-ϕ]	Measurement error [%]	STAYSL adjusted χ^2 contribution	Percent error [%]	5%–95% activation energy range [MeV]
^{197}Au(n,2n)^{196}Au^{g+m1}-1	8.803E−13	3.90	0.3	2.3	13.2–14.4
^{197}Au(n,g)^{198}Au-1	9.017E−13	2.10	0.1	0.7	5E−8–0.60
^{58}Ni(n,2n)^{57}Ni	9.543E−15	5.50	1.1	−5.7	13.6–14.5
^{58}Ni(n,p)^{58}Co^{g+m1}	2.040E−13	2.00	2.0	3.6	2.9–14.3
^{113}In(n,n′)^{113}In^{m1}	1.098E−13	2.40	0.6	−1.9	0.92–14.2
^{115}In(n,n′)^{115}In^{m1}	1.439E−13	5.60	2.1	−8.2	0.84–14.2
^{115}In(n,g)^{116}In^{m1}	1.272E−12	3.40	0.0	−0.5	5E−8–0.84
^{27}Al(n,a)^{24}Na	5.082E−14	2.10	0.6	1.7	12–14.4
^{46}Ti(n,2n)^{45}Ti	6.482E−15	2.70	8.5	−20.9	13.8–14.5
^{46}Ti(n,p)^{46}Sc	1.120E−13	2.40	1.7	4.2	7.4–14.4
^{47}Ti(n,x)^{46}Sc	1.412E−14	2.40	0.7	6.4	13.6–14.5
^{47}Ti(n,p)^{47}Sc	6.662E−14	2.60	0.7	−3.5	2.9–14.4
^{48}Ti(n,x)^{47}Sc	2.568E−15	2.60	0.0	−0.7	13.6–14.4
^{48}Ti(n,p)^{48}Sc	2.603E−14	2.30	0.0	−0.5	12.8–14.4
^{49}Ti(n,x)^{48}Sc	1.174E−15	2.30	1.7	16.0	13.6–14.5
^{186}W(n,g)^{187}W	2.000E−13	3.30	1.9	4.6	2.3E−8–1.0
^{90}Zr(n,2n)^{89}Zr	2.382E−13	2.30	0.3	−1.2	13.6–14.4
^{24}Mg(n,p)^{24}Na	8.392E−14	2.30	3.6	−4.3	11–14.4
^{197}Au(n,2n)^{196}Au^{g+m1}-2	8.450E−13	8.40	0.1	2.6	13.2–14.4
^{197}Au(n,g)^{198}Au-2	1.156E−12	2.00	0.3	−1.1	5E−8–0.50

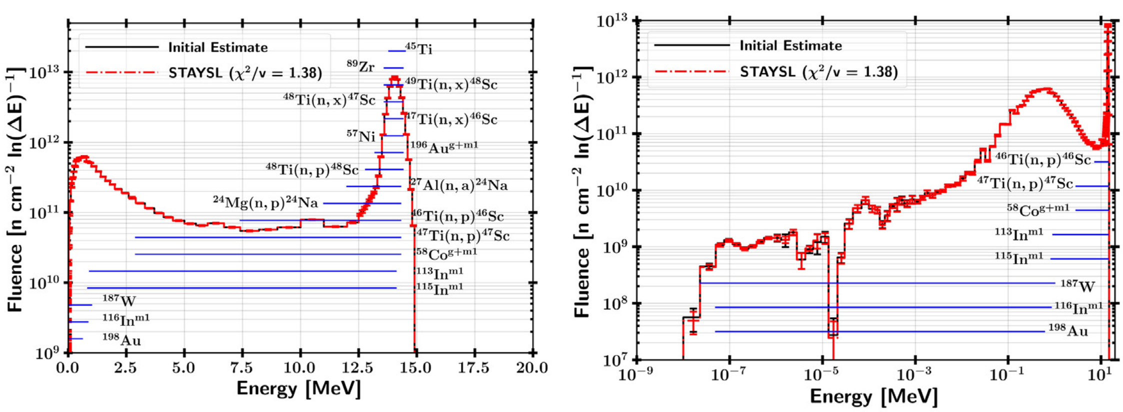

(a) Linear Energy Scale

(b) Logarithmic Energy Scale

Fig. 6. (Color online) STAYSL unfolded ATHENA internal drawer neutron spectrum for the validation shot with (a) linear and (b) logarithmic energy scales. The blue horizontal lines indicate the 5 to 95% activation range where the activation product informs the unfolded neutron spectrum.

where the neutron fluence, $\Phi(E)$, is convolved with $F_{D,\mathrm{Si}}$ and normalized by a reference value of 95 MeV−mb for the 1 MeV neutron damage function. $F_{D,\mathrm{Si}}$ was calculated using the ASTM standard for ENDF/B-VIII.0 cross-sections in natural silicon using the Robinson energy partition function [11]. Additionally, the hardness of a spectrum, which signifies the representative energy of a neutron spectrum for irradiation, is scaled by the integral of $\Phi(E)$ over all energies with

$$H_{1-\mathrm{MeV,Si}} = \frac{\Phi_{eq,1-\mathrm{MeV,Si}}}{\int_0^\infty \Phi(E)dE}. \tag{2}$$

Similarly, the Nortgett, Robinson, and Torrens (NRT) damage energy normalization can be used to account for the threshold recoiling ion energy to cause a displacement, E_d, from a lattice site [52]. The NRT damage energy was provided and calculated in the same manner as ASTM 722–19 but includes integrating over the threshold required to produce a Frenkel pair in the lattice [53,54]. The ASTM 722–19 displacement kerma and NRT damage energy function are shown in Fig. 7 for comparison.

Under NRT, $2E_d/\beta$ of incident neutron energy is required to produce a Frenkel pair, where 20.5 eV was used as an experimentally measured angular-integrated reference for E_d [55]. β is an displacement efficiency term empirically determined to be 0.8 [52]. The NRT damage energy also can be scaled to quantify the initial Frenkel pair density from displaced atoms by multiplying by $\beta/\ 2E_d$, which correlates with the displacements per atom (DPA) in a material [53,56]. Second order and more complicated defect structures are also present under neutron irradiation in silicon and should be considered for a more in depth analysis, one reason that a spectrally-accurate experimental environment such as ATHENA fills a gap in the radiation effects community [57].

Table 3 provides a summary of the irradiation environments on the ATHENA platform calculated with the methods provided above. The NIF source was modeled at a strength of 1×10^{16} neutrons, where the PDXP sources used for ATHENA are capable of producing source yields from approximately 10^{15} to 2×10^{16} neutrons with a ion temperature near 10 keV [10].

Additionally, the uncertainty term for the NRT damage energy was determined using the covariance information in the formulation derived at Sandia National Laboratories [53]. Uncertainty was taken in the damage response function for nuclear data, threshold E_d, displacement model, interaction potential, and model defects such as non-negative constraints. The covariance matrix was only derived for ^{28}Si, which is the dominant silicon natural isotope. This uncertainty can also be used as a lower estimate for the integral initial Frenkel pair density.

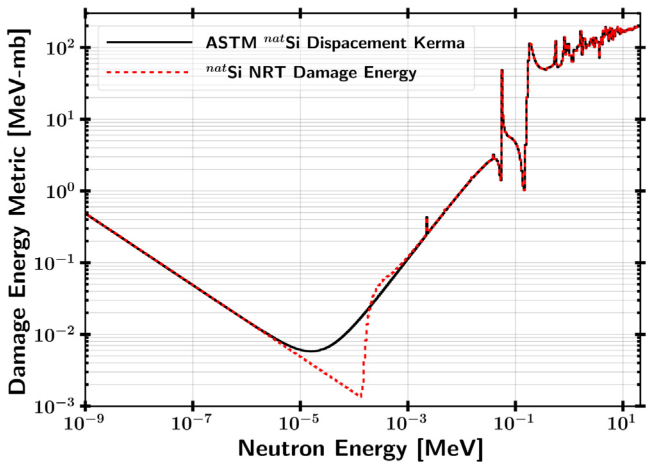

Fig. 7. (Color online) ASTM 722–19 and the NRT damage energy functions. The NRT damage energy exhibits a reduction for contributing reaction channels below the threshold energy. At energies above the NRT threshold, there is no difference.

Table 3
ATHENA irradiation position neutron environment metrics for a 10^{16} neutron shot yield.

Position	Drawer cavity	Center internal cavity	External
Φ $[\frac{n}{cm^2}]$	3.61E+12	2.32E+12	1.00E+12
$\Phi_{eq,1-MeV,Si}$ $[\frac{n}{cm^2}]$	3.64E+12	1.99E+12	1.75E+12
NRT damage energy [MeV-mb]	3.46E+14 ±11.2%	1.90E+14 ±11.6%	1.66E+14 ±16.4%
Integral Si Frenkel pairs $[\frac{\#}{\mu m^3}]$	337	185	162
$H_{1-\mathrm{MeV,Si}}$	1.0	0.90	1.75
Neutron Pulse length [ns]	50	50	10
Prompt Rad(Si)–(γ/e^-)	620	170	31
Total Rad(Si)–(γ/e^-)	630	238	133

The uniformity of the internal neutron spectrum is demonstrated by the similar values of $H_{1-\mathrm{MeV,Si}}$. As noted in Section 3.2, the thermal neutron proportion of the neutron spectrum increases father back in the cavity resulting in the lower $H_{1-\mathrm{MeV,Si}}$ for the center internal cavity. Fig. 8 highlights the general uniformity of the neutron fluence and $H_{1-\mathrm{MeV,Si}}$ over the internal cavity volume. The largest radial difference in Φ was 3% for a centered, 2.5 cm radius sample, and 7% for a maximum 3.7 cm radius.

3.3. Gamma environment

The ionizing radiation environment was modeled at each position in MCNP6 with integral validation using TLD reference doses. The MCNP6 model in Section 3.2 was used to model secondary γ-ray and electron energy deposition. Three sources of ionizing radiation were assessed for the ATHENA platform at the NIF: inelastic neutron reactions, activation decay radiation, and γ-rays produced in the D-T fusion reactions. The prompt ATHENA secondary γ-ray population was created through inelastic nuclear reactions between the higher energy incident neutrons throughout the assembly. The decay radiation produced through activation of the materials within the NIF and ATHENA platform was modeled with a four-hour integration time including all delayed particle half-lives. The 16.67 MeV γ-rays associated with the $4.2 \pm 2.0 \times 10^{-5}$ branching ratio for D-T fusion were neglected due to limited contribution to the total ionizing dose, approximately 1 mRad(Si) internally and 0.2 Rad(Si) in the external position [58]. Additionally, the PDXP source does not utilize a hohlraum, which limits the mass in the vicinity near the source, and decreases the source-associated secondary γ-ray production [59].

An electron energy deposition tally was used to estimate the expected ionizing dose from the incident particles to account for a lack of charge equilibrium. Electrons were created in the model using the default physics packages including production by γ-rays, coherent scattering, bremsstrahlung, straggling, and a 1 keV electron energy cutoff [17].

The modeled integral dose from electron energy deposition was 290 ± 4.6% rad(TLD-400) for the internal ATHENA spectrum validation shot and included contributions from decay radiation and inelastic reactions. The ionizing dose calculated with γ-ray energy deposition was 329 ± 0.1% rad(TLD-400), in general agreement with the electron results. The γ-ray based dose differs from the electron due to non-equilibrium charge caused by differing material interfaces near the TLD chips.

Experimentally, four 3.2 × 3.2 × 0.89 mm Thermo Fisher Scientific TLD-400 chips, with a manufacturer stated accuracy of ±30%, were irradiated in the internal drawer of ATHENA [60]. Four Thermo Fisher Scientific TLD-400 chips were exposed to 500 and 1000 rad(TLD-400) from a reference ^{60}Co γ-ray irradiation at an exposure rate of 54 rad(TLD-400)/minute. Each set of TLDs was measured with a Harshaw 3500 TLD reader, and the integral of the thermoluminescent (TL) curve was used to provide a measurement of the ionizing dose, scaled by a reference light efficiency. The manufacturer recommended time–temperature profile (preheat to 50 °C, followed by a 20 s acquisition of counts with a temperature rate of 25 °C/s and a maximum temperature of 400 °C) was used to heat the TLD-400 chips. The 500 and 1000 rad reference exposures were confirmed to have a linear response between counts and dose to within 1%.

The measured ionizing radiation dose was 515 ± 7.9% rad(TLD-400), 77% higher than the modeled estimate. Multiple sources possibly contribute to this disagreement. First, the manufacturer stated TLD accuracy, 30%, plays a role. Second, the exotic components inside ATHENA have little experimental data for inelastic neutron cross sections and secondary γ-ray production, and (n,xγ) reactions have been identified as a broad nuclear data need for experimental data collection [61]. This is especially important to ATHENA as there is essentially zero contribution to the ionizing dose from prompt source γ-rays, thereby increasing the relative sensitivity to secondary γ-ray production. Discrepancies have been observed between evaluated inelastic γ-ray producing cross sections and experimental observations for the principal spectral shaping components of zirconium [62], carbon [63], tungsten [64], and compositions of steel [65]. Recent coupled neutron and γ-ray studies have noted discrepancies between experiments and modeled γ-ray or ionizing dose environments on the order observed here [66–69].

Additionally, MCNP does not include correlations or conservation of energy on an individual interaction basis, therefore limiting the accuracy of the estimated the secondary γ-ray environment. Improvements to this treatment in MCNP include the cascading gamma-ray and multiplicity (CGM) model [70]. MCNP-PoliMi includes drastically improved event-by-event correlations and conservation of energy at each interaction, which may improve the modeled results. Similarly, the CGM option enables correlations between γ-rays produced through individual reaction channels.

A separate simulation in MCNP version 6.1.4, the last working MCNP CGM option available, was completed with CGM. The CGM model resulted in a total ionizing dose of 163 ± 8.0% rad(TLD-400), which was in less agreement than the original model. Additionally, the neutron energy spectrum and activation product production for the energy range of the PFNS was greatly suppressed in MCNP6.1.4, which did not agree with the measured activation products like MCNP6.2. Therefore, the primary results reported in this work are based on the MCNP6.2 output without CGM.

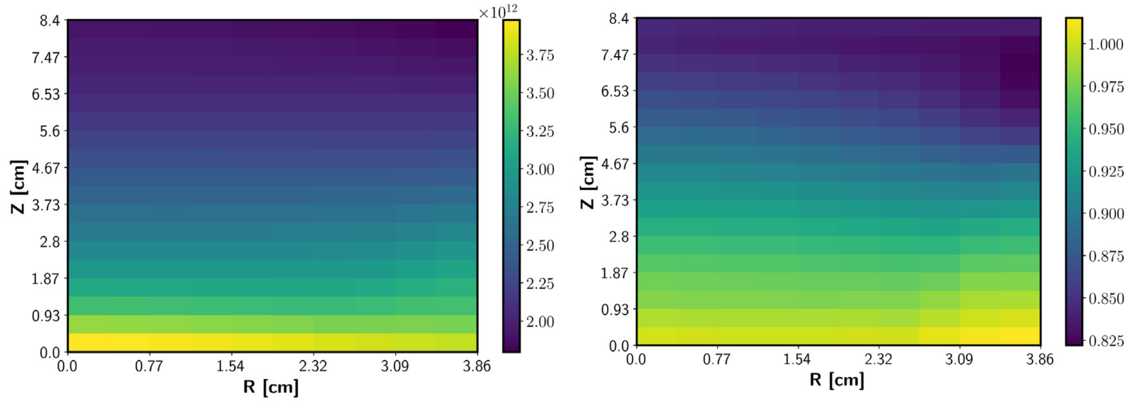

(a) Neutron fluence

(b) Spectrum hardness

Fig. 8. (Color online) Two-dimensional histogram of Φ and $H_{1-\mathrm{MeV,Si}}$ within the internal cavity volume. Spherical divergence of Φ contributes to the reduction at larger z, while the fluence is similar radially.

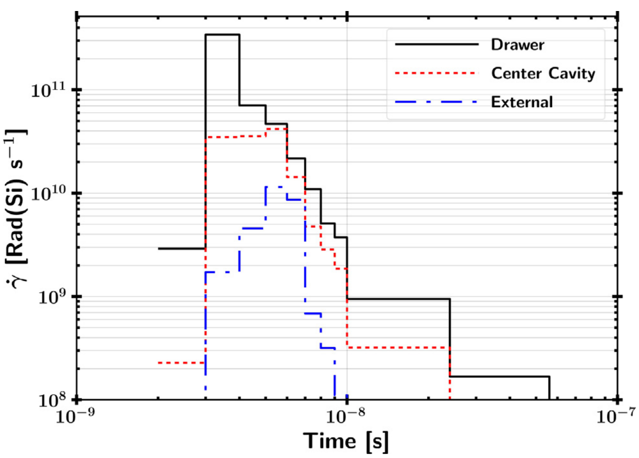

Fig. 9. (Color online) Ionization energy deposition rate in ATHENA's experimental positions for a 10^{16} neutron shot yield.

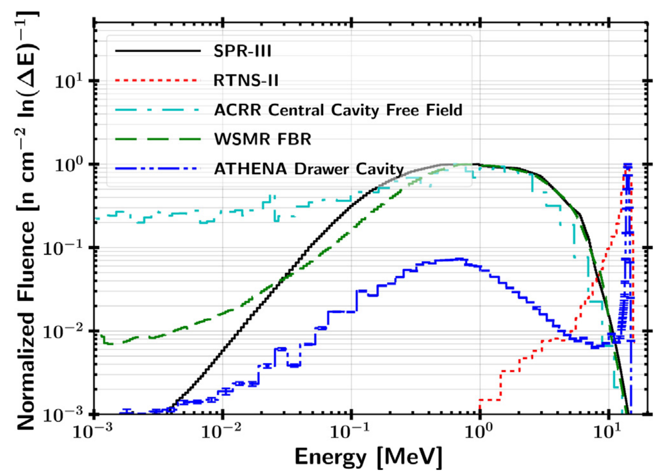

Fig. 10. (Color online) Comparison the ATHENA-I internal validation neutron energy spectrum to that of various spectra utilized for large scale radiation effects testing. Where, the ATHENA spectrum allows for a combined fission like spectrum coinciding with the high energy D-T fusion neutron component.

The integral ionizing radiation for each region outlined in Table 3 was generally too small to be relevant for effects testing. This is a benefit over traditional testing environments that are not truly a combined effects test but also have significant compounding effects from the ionizing γ-ray environment. However, the rate of the energy deposition was seen as a potential additional application to the ATHENA platform. The ATHENA modeled time-dependent dose are shown in Fig. 9 for a 10^{16} neutron shot yield, which created dose rates on the order of 10^{10} to 10^{11} Rad(Si)-s^{-1} due to the prompt nature of the modified NIF source. While ATHENA was not optimized for the γ-ray environment, this could be explored in future design modifications.

4. Application simulations

The ultimate objective of the ATHENA platform is to provide a unique radiation environment to explore the impact of the spectrum, timing, and intensity in a mixed neutron and ionizing radiation environment. As such, the ATHENA platform has several key applications and use cases for radiation effects testing and producing experimental measurements for validation of codes and nuclear data. In this section, example applications and simulations are outlined as use-cases being explored for ATHENA.

4.1. Integral nuclear data and modeling validation

Different facilities produce environments with various physics fidelity and induced nuclear test environment relevancy. Fig. 10 displays relevant U.S. testing facilities' neutron energy spectra with respect to the objective TN+PFNS. The ATHENA results indicate how this platform produces a unique environment, which spans the same energy ranges and provides capabilities within current gaps.

Additionally, the short pulse duration provides the opportunity for fission product and integral benchmarking in time-dependent, non-steady state environments. Fission product generation under a similar TN+PFNS at NIF was demonstrated in previous work is shown in Fig. 11 [1]. The R_{97} distribution is given as the activity ratio between the ith measured fission product or mass chain time-corrected atoms to the measured $A = 97$ mass chain atoms which was normalized by the ENDF-B/VIII.0 ^{235}U thermal fission product yield ratio of the ith fission product mass chain to the yield for the $A = 97$ mass chain [71].

The fission product inventories were modeled in the General Observables of Fission (GEF) code [72] in addition to semi-empirical fits to experimentally measured energy dependent fission products [73]. The reduced χ^2 for the GEF and semi-empirical fits for the entire distribution were 1.58 and 2.50, respectively.

The controlled experimental conditions provide reduced complexity and relatively rapid production of new environments by modifying ATHENA's internal materials and geometry. This allows for customized validation experiments to be conducted to supplement traditional criticality benchmarks for nuclear data evaluation and model validation

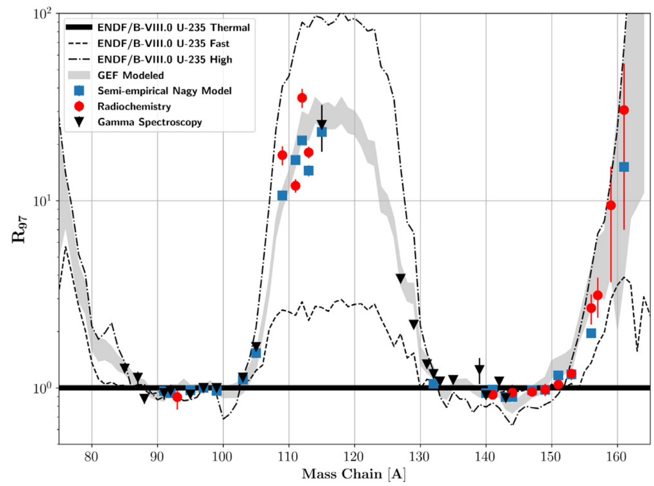

Fig. 11. (Color online) NIF ETA experiment demonstrated production of TN+PFNS fission products in highly enriched uranium sample. The modeled results were performed with the GEF code and a semi-empirical fit. ENDF-B/VIII.0 R values are provided as a reference.

suites thereby improving performance of both in non-reactor/criticality applications [74,75]. These experiments would be similar in nature to the pulse-sphere experiments, but would rely on integral measurements in a varying, and customized, environment and set of materials [76–78].

4.2. Microelectronic device environment and response

ATHENA enables experiments with a TN+PFNS on short time scales for exploring spectral and temporal impacts on the response of microelectronic components.Fig. 12 displays the neutron flux and initial Frenkel pair production rate densities in a modeled silicon sample in the ATHENA internal cavity for illustration. The neutron flux at early times is dominated by TN neutrons (red line) because of the faster velocities and less interaction time in ATHENA. At later times, the peak of the PFNS (blue line) dominates as the slower neutrons take longer time to arrive at the sample area. The Frenkel pair production is proportional to the time-dependent $\Phi_{eq,1-\mathrm{MeV,Si}}$ as described in Section 3.2.2, where the late-time lower energy neutrons (green line) contribute less to the displacement damage in a sample. The internal drawer environment is similar to the internal cavity results shown in Fig. 12, while the external experiment volume has a larger contribution from the source D-T neutrons leading the start of the defect generation.

Compared with current facilities, the ATHENA platform offers a different radiation spectrum with a short-pulse (≤50 ns) capability. Larger device damage rates and magnitudes could be achieved at the NIF without spectral modification; however, the neutron energy spectrum produced can be used to explore and validate spectral equivalency models commonly used for radiation effects on electronics. The combination of a tunable, prompt neutron environment with spectral and timing characteristics not available anywhere else in the world allows ATHENA to be used for unique validation experiments for time-evolution of defects in semiconductor materials and microelectronic device response.

4.2.1. Defect characterization

ATHENA offers unique environments to explore defect types and concentrations as a function of time and spectral intensity. To illustrate the differences in defects in Si from different irradiation environments, a model was adopted from mean field theory [79]. Si was chosen because of the extensive literature and experimental history.

A coupled system of ordinary differential equations was created describing the formation of concentrations of point defects including

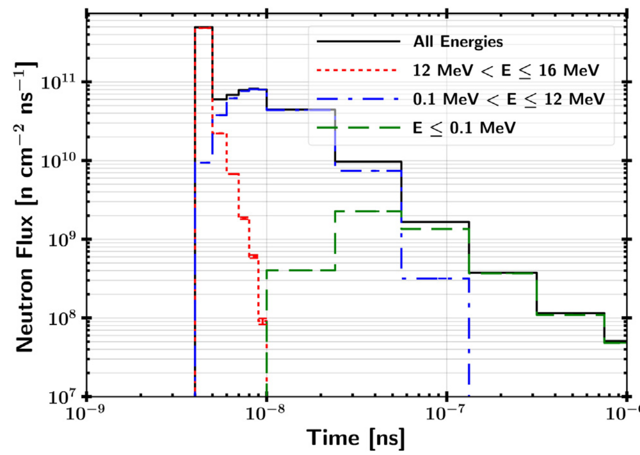

Fig. 12. (Color online) Internal ATHENA environment neutron flux for a 10^{16} neutron shot yield.

Table 4
Mean field theory model parameters [80–85].

Parameter	Symbol	Value
Temperature	T	300 K
Boltzmann constant	k_b	8.617E−5 eV/K
Atomic volume	V_{at}	0.02 nm^3
Burgers vector	b	0.384 nm
Vacancy formation energy	E_f^v	3.96 eV
Interstitial formation energy	E_f^i	3.8 eV
Hop Frequency	υ	1E12 Hz
Hop distance	d	0.235 nm
Vacancy diffusion prefactor	D_o^v	5.52E10 nm^2 s^{-1}
Interstitial diffusion prefactor	D_i^v	5.52E10 nm^2 s^{-1}
Vacancy migration energy	E_m^v	0.35 eV
Interstitial migration energy	E_m^i	0.07 eV
Di-vacancy binding energy	$E_b^{2v} = E_f^v - E_f^{2v}$	2.4 eV
Di-interstitial binding energy	$E_b^{2i} = 2E_f^i - E_f^{2i}$	1.9 eV
Dose rate	Γ(t)	Varied
The cascade efficiency	η	0.4
The fraction of point defects Produced during irradiation	ϵ_{PD}	1
Recombination coefficient	$\mu_R = \frac{4\pi(r_i+r_v)}{V_{at}}$	277 nm^{-2}
Dislocation density	ρ_d	3E−4 nm^{-2}
Capture efficiency for SIA clusters	Z_i	1.2

interstitial Si atoms, C_{int}, and vacancies, C_v. Additionally, size n clusters of interstitial, $C_{int,n}$, and vacancy, $C_{v,n}$, concentrations up to n=9 were tracked for convergence with $C_{v,10} = C_{int,10} = 0$. For simplicity, it was assumed that the radiation only produces point defects, that point defects are the only mobile species, and that all clusters are immobile.

The system of differential equations was first discretized by implementing implicit time-stepping and the resulting discrete equations were solved iteratively using the Newton–Raphson method. The concentration of defects was tracked throughout the irradiation of ATHENA's internal cavity as described in Sections 3.2 and 4.2 . A reference case with a constant 10^{-5} DPA-s^{-1} for an integral 4.5×10^{-6} DPA, analogous to longer period nuclear reactor irradiations, was selected for comparison to ATHENA at an integral 3.6×10^{-9} DPA. The resulting summation of all cluster sizes are shown in Fig. 13, where the model parameters required are summarized in Table 4.

The modeled vacancy and interstitial distributions highlight that short-pulse neutron environments, where the crystal lattice is not allowed to relax to equilibrium between events, can produce drastically different results in the observable defect concentrations. In the ATHENA internal cavity results, recombination is less prevalent at these short time scales, as the population of interstitial sites does not equilibrate prior to the creation of additional defects. The net result

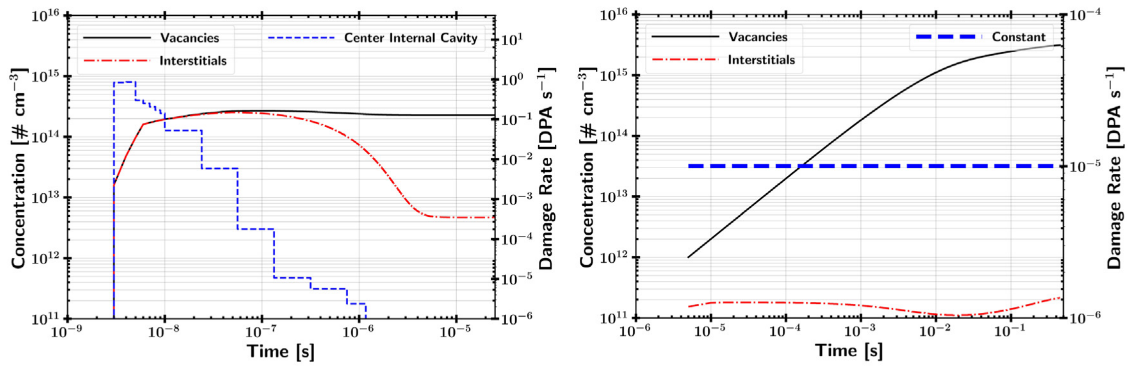

(a) NIF ATHENA Internal Cavity

(b) Constant 10^{-5} DPA-s^{-1}

Fig. 13. (Color online) Mean field theory results for the summation of all cluster sizes of interstitial (sum of C_{int} through $C_{int,9}$) and vacancy (sum of C_v through $C_{v,9}$) defects for the (a) ATHENA internal cavity with an integral 3.6×10^{-9} and (b) constant displacement damage rate with an integral 4.5×10^{-6} DPA, showing that the temporal aspects to an irradiation can create significantly different defect concentrations in the device.

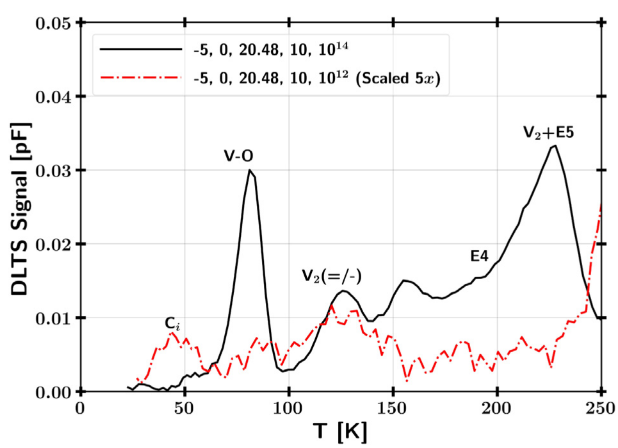

Fig. 14. (Color online) DLTS base-collector measurements of 2N2222 devices irradiated at the OSURR showing the major electron traps and associated identified defect formations. Non-identified peaks correspond to hydrogen-related defect complexes. The DLTS labels correspond to the device reverse bias [V], pulsing bias [V], rate window [ms], and pulse width [ms], and $\Phi_{eq,1-\mathrm{MeV,Si}}$ [$\frac{\mathrm{n}}{\mathrm{cm}^2}$], respectively.

increases the proportion of interstitial sites post-irradiation compared to the case of the fixed dose rate relevant to longer irradiation pulses, where the interstitials have a longer time period to recombine and reach an approximately steady-state distribution. Additionally,

Experimentally, sample 2N2222 bipolar junction transistor (BJT) devices were irradiated at the Ohio State University Research Reactor (OSURR) to demonstrate the observable defects between $\Phi_{eq,1-\mathrm{MeV,Si}}$ of 10^{12} to 10^{14} $\frac{\mathrm{n}}{\mathrm{cm}^2}$. Deep-level transient spectroscopy (DLTS) was performed on the devices to characterize the charge carrier traps. The DLTS measurements are provided in Fig. 14.

Electron traps included interstitial carbon, C_i, vacancy-oxygen pairs, $V-O$, di-vacancy centers, $V_2(=\ /-)$, $E4$ centers, and $E5$ centers. Although the defect concentration is predicted to be low, defects were able to be measured at similar $\Phi_{eq,1-\mathrm{MeV,Si}}$ levels to the expected ATHENA environment. The $\Phi_{eq,1-\mathrm{MeV,Si}}$ of 10^{14} $\frac{\mathrm{n}}{\mathrm{cm}^2}$ was used to help resolve the scaled $\Phi_{eq,1-\mathrm{MeV,Si}}$ of 10^{12} $\frac{\mathrm{n}}{\mathrm{cm}^2}$ environment, where there was shown to be a non-linear growth of the traps.

4.2.2. BJT device response

The device response of components such as a silicon-based BJT is dependent on the radiation environment. Testing of these types of devices under different conditions is important to determine the response of the device to assess performance in a radiation environment. Originally posed by Messenger and Spratt [86], the current gain before irradiation, β_0, and after irradiation, β_f, of a transistor can be described by a linear relationship to the total fluence under a given neutron spectrum, $\Phi(E)$, given by,

$$\frac{1}{\beta_f} = \frac{1}{\beta_i} + K(E)\Phi(E), \tag{3}$$

where a proportionality constant, $K(E)$, can be defined for a particular device and environment. During irradiation, the Frenkel pair defect generation can create band levels below the conduction band for Si. The defects ultimately reduce device performance by reducing carrier lifetimes through reduction of mobility, leading to gain degradation.

Short irradiation pulses result in non-equilibrium defect generation and present a different set of environmental conditions that can result in a different observable effect in device response. $K(E)$ has been shown experimentally to be a function of the radiation flux environment, where larger flux rates lead to higher damage coefficients [87]. Larger fluxes lead to more severe short-term damage under fast-burst fission reactor conditions; however, BJT devices sustained less damage after long term annealing. Higher initial damage in high flux environments is likely due to a combination of metastable defect states and shorter annealing time [87]. Additionally, the suppressed damage after long annealing times is possibly linked to higher concentrations of interstitial and vacancy sites, leading to higher levels of recombination before stable defects can form.

Fig. 15 highlights a few radiation effects testing sources in comparison to the ATHENA environment. Testing environments are relevant to different nuclear scenarios, where each exists to test different corners of the domain. Characterizing different calibration points is essential to validate pre-dominant semi-empirical models used to assess device performance under neutron and surrogate neutron irradiation. Increasing testing of the space can increase confidence in predictive models that allow enhanced confidence to interpolate and extrapolate into environments where testing is not currently feasible. Furthermore, having a flexible testing capability to inform first-principle models is essential as devices deviate farther from historical testing data and to new device architectures [88]. Smaller physical size as well as drift BJTs have been shown to deviate from the original implementation of the Messenger-Spratt relationship [89,90].

5. Conclusion and perspectives

The ATHENA platform has been designed as a flexible spectral modification platform with a capability to act as a short-pulse neutron and intense γ dose rate source at NIF. Coupled with data available at currently operational facilities, the ATHENA prompt thermonuclear and prompt fission spectrum environment increases the environmental domain to test devices and validate nuclear data and physics models

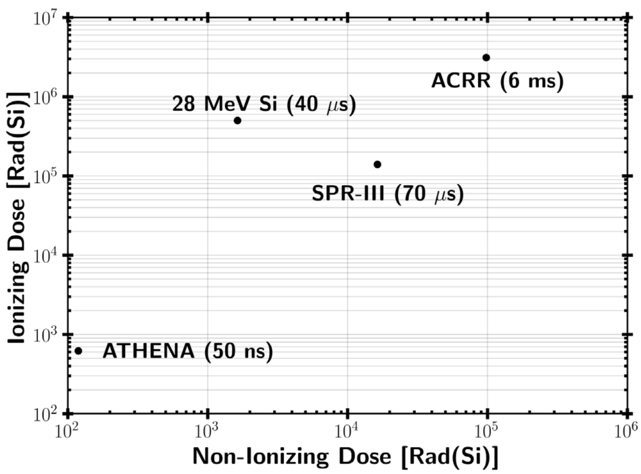

Fig. 15. ATHENA internal environment characteristics in comparison to the ACRR, SPR-III, and representative 28 MeV Si ion beam [9,12,14]. The neutron pulse length for each environment are provided highlighting that ATHENA enables an experimental condition with a TN+PFNS in prompt time scales.

in a highly-controlled facility platform. ATHENA also provides updates from the ETA platform for an expanded diagnostic region, which is essential for active experimentation on electronics components or with detector systems, and a secondary external platform for direct comparisons between environment conditions.

Integral validation of the ATHENA internal radiation environment provided a clearer understanding of the experimental capabilities and uncertainty analysis of the platform. The environment was modeled in MCNP6 using ENDF-B/VIII.0 and IRDFF v.1.05 nuclear data libraries with systematic nuclear data uncertainties calculated through stochastic sampling in SCALE Sampler using an ensemble of 300 realizations of the 1597-group ENDF-B/VIII.0 library. A total of 20 activation products were measured at the initial validation shot, and the reduced χ^2 was = 1.38, indicating general agreement with the modeled results. The total ionizing dose was measured to be 515 ± 7.9% rad(TLD-400), whereas the modeled values indicated a lower value of 290 ± 4.6% rad(TLD-400). The discrepancy requires additional research to determine the origin as being dominated by either nuclear data and radiation transport models or measurement.

Future work on the ATHENA platform will be scoped to test 2N2222 BJT devices at NIF. These components have a extensive history of radiation environment characterization, and they offer a starting benchmark experiment before moving toward more exotic devices. The ATHENA platform's utility lies in the unique calibration point to validate models for surrogate sources and enhance understanding of radiation effects experiments.

CRediT authorship contribution statement

Nicholas J. Quartemont: Conceptualization, Methodology, Software, Validation, Formal analysis, Investigation, Data curation, Writing – original draft, Visualization. **George Peterson:** Conceptualization, Investigation, Visualization. **Colton Moran:** Conceptualization, Visualization. **Adib Samin:** Conceptualization, Methodology, Writing – review & editing, Formal analysis. **Buguo Wang:** Conceptualization, Formal analysis, Methodology, Writing – review & editing. **Charles Yeamans:** Investigation, Writing – review & editing, Project administration. **Brandon Woodworth:** Investigation, Project administration. **Darren Holland:** Writing – review & editing. **James C. Petrosky:** Supervision. **James E. Bevins:** Writing – review & editing, Supervision, Funding acquisition, Project administration.

Declaration of competing interest

The authors declare that they have no known competing financial interests or personal relationships that could have appeared to influence the work reported in this paper.

Acknowledgments

This work is supported by the National Nuclear Security Administration (NNSA) under grant NA000103 and the Defense Threat Reduction Agency under grant HDTRA-1033292. Some of this work was performed under the auspices of the U.S. Department of Energy by Lawrence Livermore National Laboratory under Contract DE-AC52-07NA27344. The views expressed in this article are those of the authors and do not necessarily reflect the official policy or position of the United States Air Force, the Department of Defense, or the United States Government.

Additionally, the authors would like to thank Todd Woody, Keenan Thomas, Sam Glover, and Brent Blue (Lawrence Livermore National Laboratory), Cihangir Celik and William Wieselquist (Oak Ridge National Laboratory), and Pat Griffin (Sandia National Laboratories) for their invaluable support of this research.

References

[1] N. Quartemont, N. Gharibyan, K. Moody, J. Bevins, Uranium integral fission product yields for a spectrally-shaped 14.1 MeV neutron source at the national ignition facility, Appl. Radiat. Isot. (2021) 109711, http://dx.doi.org/10.1016/j.apradiso.2021.109711, URL https://www.sciencedirect.com/science/article/pii/S0969804321001184.

[2] N.J. Quartemont, A.A. Bickley, J.E. Bevins, Nuclear data covariance analysis in radiation transport simulations utilizing SCALE sampler and the IRDFF nuclear data library, IEEE Trans. Nucl. Sci. 67 (3) (2020) 482–491, http://dx.doi.org/10.1109/TNS.2020.2970700, arXiv:https://doi.org/10.1109/TNS.2020.2970700.

[3] J. Bevins, Targeted Modification of Neutron Energy Spectra for National Security Applications (Ph.D. thesis), University of California, Berkeley, 2017.

[4] J.E. Bevins, Z. Sweger, N. Munshi, B. Goldblum, J. Brown, D. Bleuel, L. Bernstein, R. Slaybaugh, Performance evaluation of an energy tuning assembly for neutron spectral shaping, Nucl. Instrum. Methods Phys. Res. A 923 (2019) 79–87, http://dx.doi.org/10.1016/j.nima.2019.01.049, arXiv:https://doi.org/10.1016/j.nima.2019.01.049.

[5] A. Kahler, R. MacFarlane, R. Mosteller, B. Kiedrowski, S. Frankle, M. Chadwick, R. McKnight, R. Lell, G. Palmiotti, H. Hiruta, M. Herman, R. Arcilla, S. Mughabghab, J. Sublet, A. Trkov, T. Trumbull, M. Dunn, ENDF/B-VII.1 neutron cross section data testing with critical assembly benchmarks and reactor experiments, Nucl. Data Sheets 112 (12) (2011) 2997–3036, http://dx.doi.org/10.1016/j.nds.2011.11.003, Special Issue on ENDF/B-VII.1 Library. URL https://www.sciencedirect.com/science/article/pii/S0090375211001141.

[6] H. Choi, G. Roh, Benchmarking MCNP and WIMS/RFSP against measurement data—I: Deuterium critical assembly, Nucl. Sci. Eng. 146 (2) (2004) 188–199, http://dx.doi.org/10.13182/NSE04-A2402, arXiv:https://doi.org/10.13182/NSE04-A2402.

[7] Joint Defense Science Board/Threat Reduction Advisory Comittee Task Force, The Nuclear Weapons Effects National Enterprise, Tech. rep., Office of the Under Secretary of Defense for Acquisition, Technology, and Logistics, Washington, DC, 2010.

[8] D.B. King, R.M. Fleming, E.S. Bielejec, J.K. McDonald, G. Vizkelethy, Test simulation of neutron damage to electronic components using accelerator facilities, Nucl. Instrum. Methods Phys. Res. B 365 (2015) 294–299, http://dx.doi.org/10.1016/j.nimb.2015.08.026.

[9] J.G. (Jake) Kelly, P.J. Griffin, W.C. Fan, Benchmarking the sandia pulsed reactor III cavity neutron spectrum for electronic parts calibration and testing, IEEE Trans. Nucl. Sci. 40 (6) (1993) 1418–1425, http://dx.doi.org/10.1109/23.273523.

[10] C.B. Yeamans, D.L. Bleuel, The spatially distributed neutron activation diagnostic FNADs at the national ignition facility, Fusion Sci. Technol. 72 (2) (2017) 120–128, http://dx.doi.org/10.1080/15361055.2017.1320499, arXiv:https://doi.org/10.1080/15361055.2017.1320499.

[11] ASTM Standard E772-19, Standard Practice for Characterizing Neutron Fluence Spectra in Terms of an Equivalent Monoenergetic Neutron Fluence for Radiation-Hardness Testing of Electronics, Standard, ASTM International, West Conshohocken, PA, 2019.

[12] P. Griffin, D. King, N. Kolb, Application of spallation neutron sources in support of radiation hardness studies, Nucl. Instrum. Methods Phys. Res. A 562 (2) (2006) 684–687, http://dx.doi.org/10.1016/j.nima.2006.02.021.

[13] E. Bielejec, G. Vizkelethy, R.M. Fleming, D.B. King, Metrics for comparison between displacement damage due to ion beam and neutron irradiation in silicon BJTs, IEEE Trans. Nucl. Sci. 54 (6) (2007) 2282–2287, http://dx.doi.org/10.1109/TNS.2007.909513.
[14] E.J. Parma, G.E. Naranjo, R.M. Vega, L.L. Lippert, D.W. Vehar, P.J. Griffin, Radiation Characterization Summary: ACRR Central Cavity Free-Field Environment with the 32-Inch Pedestal at the Core Centerline (ACRR-FF-CC-32-cl), Tech. rep., Sandia National Laboratory, Albuquerque, NM, 2015.
[15] N.J. Quartemont, NIF ATHENA experiment, 2021, http://dx.doi.org/10.17632/shf56c665r.1, URL http://dx.doi.org/10.17632/bnvh2btjp3.1.
[16] J.E. Bevins, R.N. Slaybaugh, Gnowee: A hybrid metaheuristic optimization algorithm for constrained, black box, combinatorial mixed-integer design, Nucl. Technol. 205 (4) (2019) 542–562, http://dx.doi.org/10.1080/00295450.2018.1496692, arXiv:https://doi.org/10.1080/00295450.2018.1496692.
[17] C.J. Werner, et al., MCNP6.2 Release Notes, report LA-UR-18-20808, Los Alamos National Laboratory, 2018.
[18] H. Paxton, N.L. Pruvost, Critical Dimensions of Systems Containing 235U, 239Pu, and 233U, Tech. rep., Los Alamos National Laboratory, Los Alamos, NM, 1987.
[19] R. Capote, K. Zolotarev, V. Pronyaev, A. Trkov, International reactor dosimetry and fusion file IRDFF v.1.05, J. ASTM Int. 9 (4) (2012).
[20] H. Xiaolong, Nuclear data sheets for A = 196, Nucl. Data Sheets 108 (2007) 1093–1286, http://dx.doi.org/10.1016/j.nds.2007.05.001, arXiv:https://doi.org/10.1016/j.nds.2007.05.001.
[21] X. Huang, M. Kang, Nuclear data sheets for A = 198, Nucl. Data Sheets 133 (2016) 221–416, http://dx.doi.org/10.1016/j.nds.2016.02.002, arXiv:https://doi.org/10.1016/j.nds.2016.02.002.
[22] M.R. Bhat, Nuclear data sheets for A = 57, Nucl. Data Sheets 85 (1998) 415–536, http://dx.doi.org/10.1016/j.ssc.2010.07.050, arXiv:https://doi.org/10.1006/ndsh.1998.0021.
[23] C.D. Nesaraja, S.D. Geraedts, B. Singh, Nuclear data sheets for A = 58, Nucl. Data Sheets 111 (2010) 897–1092, http://dx.doi.org/10.1016/j.nds.2010.03.003, arXiv:http://dx.doi.org/10.1016/j.nds.2010.03.003.
[24] J. Blachot, Nuclear data sheets for A = 113, Nucl. Data Sheets 111 (2010) 1471–1618, http://dx.doi.org/10.1016/j.nds.2010.05.001, arXiv:http://dx.doi.org/10.1016/j.nds.2010.05.001.
[25] J. Blachot, Nuclear data sheets for A = 115, Nucl. Data Sheets 113 (2012) 2391–2535, http://dx.doi.org/10.1016/j.nds.2012.10.002, arXiv:http://dx.doi.org/10.1016/j.nds.2012.10.002.
[26] J. Blachot, Nuclear data sheets for A = 116, Nucl. Data Sheets 111 (2010) 717–895, http://dx.doi.org/10.1016/j.nds.2010.03.002, arXiv:http://dx.doi.org/10.1016/j.nds.2010.05.001, URL http://dx.doi.org/10.1016/j.nds.2010.05.001.
[27] R.B. Firestone, Nuclear data sheets for A = 24, Nucl. Data Sheets 108 (2007) 2319–2392, http://dx.doi.org/10.1016/j.nds.2007.10.001, arXiv:https://doi.org/10.1016/j.nds.2007.10.001.
[28] T. Burrows, Nuclear data sheets for A = 45, Nucl. Data Sheets 109 (1) (2008) 171–296, http://dx.doi.org/10.1016/j.nds.2007.12.002, URL https://www.sciencedirect.com/science/article/pii/S0090375207001147.
[29] S.-C. Wu, Nuclear data sheets for A = 46, Nucl. Data Sheets 91 (1) (2000) 1–116, http://dx.doi.org/10.1006/ndsh.2000.0014, URL https://www.sciencedirect.com/science/article/pii/S0090375200900140.
[30] T. Burrows, Nuclear data sheets for A = 47, Nucl. Data Sheets 108 (5) (2007) 923–1056, http://dx.doi.org/10.1016/j.nds.2007.04.002, URL https://www.sciencedirect.com/science/article/pii/S0090375207000403.
[31] T. Burrows, Nuclear data sheets for A = 48, Nucl. Data Sheets 107 (7) (2006) 1747–1922, http://dx.doi.org/10.1016/j.nds.2006.05.005, URL https://www.sciencedirect.com/science/article/pii/S0090375206000482.
[32] M.S. Basunia, Nuclear data sheets for A = 187, Nucl. Data Sheets 110 (5) (2009) 999–1238, http://dx.doi.org/10.1016/j.nds.2009.04.001, arXiv:http://dx.doi.org/10.1016/j.nds.2009.04.001.
[33] B. Singh, Nuclear data sheets for A = 89, Nucl. Data Sheets 114 (2013) 1–208, http://dx.doi.org/10.1016/j.nds.2013.01.001, arXiv:http://dx.doi.org/10.1016/j.nds.2013.01.001.
[34] C.B. Yeamans, N. Gharibyan, A neutron activation spectrometer and neutronic experimental platform for the national ignition facility (invited), Rev. Sci. Instrum. 87 (11) (2016) 11D702, http://dx.doi.org/10.1063/1.4962871, arXiv:https://aip.scitation.org/doi/pdf/10.1063/1.4962871, URL https://aip.scitation.org/doi/abs/10.1063/1.4962871.
[35] R. Hatarik, D.B. Sayre, J.A. Caggiano, T. Phillips, M.J. Eckart, E.J. Bond, C. Cerjan, G.P. Grim, E.P. Hartouni, J.P. Knauer, J.M. McNaney, D.H. Munro, Analysis of the neutron time-of-flight spectra from inertial confinement fusion experiments, J. Appl. Phys. 118 (18) (2015) http://dx.doi.org/10.1063/1.4935455.
[36] F. Merrill, D. Bower, R. Buckles, D. Clark, C. Danly, O. Drury, J. Dzenitis, V. Fatherley, D. Fittinghoff, R. Gallegos, G. Grim, N. Guler, E. Loomis, S. Lutz, R. Malone, D. Martinson, D. Mares, D. Morley, G. Morgan, D. Wilson, The neutron imaging diagnostic at NIF (invited), Rev. Sci. Instrum. 83 (2012) 10D317, http://dx.doi.org/10.1063/1.4739242.
[37] B. Rearden, M. Jessee (Eds.), SCALE Code System, ORNL/TM-2005/39, Version 6.2.3, Tech. rep., Oak Ridge National Laboratory, Oak Ridge, Tennessee, 2018, arXiv:https://doi.org/10.2172/1426571.
[38] D. Brown, et al., ENDF/B-VIII.0: The 8th major release of the nuclear reaction data library with CIELO-project cross sections, new standards and thermal scattering data", Nucl. Data Sheets 148 (2018) 1–142, http://dx.doi.org/10.1016/j.nds.2018.02.001, Special Issue on Nuclear Reaction Data. arXiv:https://doi.org/10.1016/j.nds.2018.02.001, URL http://www.sciencedirect.com/science/article/pii/S0090375218300206.
[39] A. Trkov, et al., IRDFF-II: A new neutron metrology library, Nucl. Data Sheets 163 (2020) 1–108, arXiv:https://arxiv.org/abs/1909.03336v2, https://arxiv.org/abs/1909.03336v2.
[40] C.L. Ellison, H.D. Whitley, C.R.D. Brown, S.R. Copeland, W.J. Garbett, H.P. Le, M.B. Schneider, Z.B. Walters, H. Chen, J.I. Castor, R.S. Craxton, M. Gatu Johnson, E.M. Garcia, F.R. Graziani, G.E. Kemp, C.M. Krauland, P.W. McKenty, B. Lahmann, J.E. Pino, M.S. Rubery, H.A. Scott, R. Shepherd, H. Sio, Development and modeling of a polar-direct-drive exploding pusher platform at the national ignition facility, Phys. Plasmas 25 (7) (2018) 072710, http://dx.doi.org/10.1063/1.5025724, arXiv:https://doi.org/10.1063/1.5025724.
[41] C. Yeamans, G. Kemp, Z. Walters, H. Whitley, P. McKenty, E. Garcia, Y. Yang, R. Craxton, B. Blue, High yield polar direct drive fusion neutron sources at the national ignition facility, Nucl. Fusion 61 (4) (2021) 046031, http://dx.doi.org/10.1088/1741-4326/abe4e6.
[42] A.M. McEvoy, H.W. Herrmann, C.J. Horsfield, C.S. Young, E.K. Miller, J.M. Mack, Y. Kim, W. Stoeffl, M. Rubery, S. Evans, T. Sedillo, Z.A. Ali, Gamma bang time analysis at OMEGA, Rev. Sci. Instrum. 81 (10) (2010) 10D322, URL https://afit.idm.oclc.org/login?url=http://search.ebscohost.com/login.aspx?direct=true&db=asn&AN=54858034&site=eds-live.
[43] H. Brysk, Fusion neutron energies and spectra, Plasma Phys. 15 (7) (1973) 611–617, http://dx.doi.org/10.1088/0032-1028/15/7/001, arXiv:arXiv:1011.1669v3.
[44] B. Appelbe, J. Chittenden, Relativistically correct DD and DT neutron spectra, High Energy Density Phys. 11 (1) (2014) 30–35, arXiv:https://doi.org/10.1016/j.hedp.2014.01.003.
[45] C.B. Yeamans, D.L. Bleuel, The spatially distributed neutron activation diagnostic FNADs at the national ignition facility, Fusion Sci. Technol. 72 (2) (2017) 120–128, http://dx.doi.org/10.1080/15361055.2017.1320499, arXiv:https://doi.org/10.1080/15361055.2017.1320499.
[46] N. Gharibyan, K.J. Moody, J.D. Despotopulos, P.M. Grant, D.A. Shaughnessy, First fission yield measurements at the national ignition facility: 14-MeV neutron fission of 238U, J. Radioanal. Nucl. Chem. 303 (2) (2015) 1335–1338, http://dx.doi.org/10.1007/s10967-014-3474-6, arXiv:https://doi.org/10.1007/s10967-014-3474-6.
[47] B. Rooney, S. Garner, P. Felsher, P. Karpius, M. Lombardi, PeakEasy 4.99, Release LA-CC-13-040, Los Alamos, NM, 2020. URL https://PeakEasy.lanl.gov.
[48] R. Gunnink, J.B. Niday, Computerized Quantitative Analysis By Gamma-Ray Spectrometry. Vol. 1. Description of the Gamanal Program, Tech. rep., Lawrence Livermore Laboratory, Livermore, CA, 1972, arXiv:https://doi.org/10.2172/4696896.
[49] K.J. Moody, N. Gharibyan, D.A. Shaughnessy, P.M. Grant, J.M. Gostic, C.J. Cerjan, C.B. Yeamans, J.D. Despotopulos, S.A. Faye, Nuclear spectrometry of 9.6 h $^{196}Au^{m2}$ and the reaction of ^{197}Au with fast neutrons, J. Phys. G: Nucl. Part. Phys. 47 (4) (2020) 1–48, arXiv:https://doi.org/10.1088/1361-6471/ab67e9.
[50] L. Greenwood, C. Johnson, Least-squares neutron spectral adjustment with STAYSL PNNL, EPJ Web Conf. 106 (2016) 07001, http://dx.doi.org/10.1051/epjconf/201610607001, arXiv:https://doi.org/10.1051/epjconf/201610607001.
[51] K.R. Depriest, Historical Examination of the ASTM Standard E722 1-MeV Silicon Equivalent Fluence Metric, Tech. Rep. SAND2019 -15194, Sandia National Laboratories, Albuquerque, NM, 2019, http://dx.doi.org/10.2172/1592863, URL https://www.osti.gov/biblio/1592863.
[52] M.J. Norgett, M.T. Robinson, I.M. Torrens, A proposed method of calculating displacement dose rates, Nucl. Eng. Des. 33 (1) (1975) 50–54, http://dx.doi.org/10.1016/0029-5493(75)90035-7.
[53] P.J. Griffin, Uncertainty characterization of silicon damage metrics, IEEE Trans. Nucl. Sci. 66 (1) (2019) 327–336, http://dx.doi.org/10.1109/TNS.2018.2876058.
[54] P.J. Griffin, Detailed Description of the Derivation of the Silicon Damage Response Function, Tech. rep., Sanida National Laboratories, Albuquerque, NM, 2016.
[55] J. Bourgoin, P. Ludeau, B. Massarani, Threshold energy determination in thick semiconductor samples, Rev. Phys. Appl. 11 (2) (1976) 279–284, http://dx.doi.org/10.1051/rphysap:01976001102027900.
[56] M. Norgett, M. Robinson, I. Torrens, A proposed method of calculating displacement dose rates, Nucl. Eng. Des. 33 (1) (1975) 50–54, http://dx.doi.org/10.1016/0029-5493(75)90035-7, URL http://www.sciencedirect.com/science/article/pii/0029549375900357.
[57] S.M. Myers, P.J. Cooper, W.R. Wampler, Model of defect reactions and the influence of clustering in pulse-neutron-irradiated Si, J. Appl. Phys. 104 (4) (2008) http://dx.doi.org/10.1063/1.2963697.
[58] Y. Kim, et al., D-T gamma-to-neutron branching ratio determined from inertial confinement fusion plasmas, Phys. Plasmas 19 (5) (2012) 056313, http://dx.doi.org/10.1063/1.4718291, arXiv:https://doi.org/10.1063/1.4718291.
[59] H.W. Herrmann, et al., Diagnosing inertial confinement fusion gamma ray physics (invited), Rev. Sci. Instrum. 81 (10) (2010) 10D333, http://dx.doi.org/10.1063/1.3495770, arXiv:https://doi.org/10.1063/1.3495770.

[60] TLD-400™ thermoluminescent dosimetry material. URL https://www.thermofisher.com/order/catalog/product/SNO48835#/SNO48835.
[61] L.A. Bernstein, et al., Our future nuclear data needs, Annu. Rev. Nucl. Part. Sci. 69 (1) (2019) 109–136, http://dx.doi.org/10.1146/annurev-nucl-101918-023708, arXiv:https://doi.org/10.1146/annurev-nucl-101918-023708.
[62] S. Zhang, et al., Measurement of leakage neutron spectra for zirconium with D-T neutrons and validation of evaluated nuclear data, Fusion Eng. Des. 149 (2019) 111311, http://dx.doi.org/10.1016/j.fusengdes.2019.111311, URL https://www.sciencedirect.com/science/article/pii/S0920379619307975.
[63] M.A. Norsworthy, et al., Light output response of EJ-309 liquid organic scintillator to 2.86–3.95 MeV carbon recoil ions due to neutron elastic and inelastic scatter, Nucl. Instrum. Methods Phys. Res. A 884 (2018) 82–91, http://dx.doi.org/10.1016/j.nima.2017.11.084, URL https://www.sciencedirect.com/science/article/pii/S0168900217313359.
[64] G. Henning, et al., Measurement of 182,184,186w (n, n´ oss sections and what we can learn from it, EPJ Web Conf. 247 (2021) 09003, http://dx.doi.org/10.1051/epjconf/202124709003.
[65] C.E. Romano, et al., Discussion session highlights, in: Proceedings of the Workshop for Applied Nuclear Data: WANDA 2020, 2020, pp. 10–12, http://dx.doi.org/10.2172/1649010, URL https://www.osti.gov/biblio/1649010.
[66] A. Murari, et al., Measuring the radiation field and radiation hard detectors at JET: Recent developments, Nucl. Instrum. Methods Phys. Res. A 593 (3) (2008) 492–504, http://dx.doi.org/10.1016/j.nima.2008.05.058.
[67] A. Negret, et al., Cross-section measurements for the Fe 56 (n, xnγ) reactions, Phys. Rev. C 90 (3) (2014) 1–15, http://dx.doi.org/10.1103/PhysRevC.90.034602.
[68] M.L. Mauborgne, et al., Designing tools for oil exploration using nuclear modeling, EPJ Web Conf. 146 (2017) 4–7, http://dx.doi.org/10.1051/epjconf/201714609036.
[69] M. Kerveno, et al., From γ emissions to (n,xn) cross sections of interest: The role of GAINS and GRAPhEME in nuclear reaction modeling, Eur. Phys. J. A 51 (12) (2015) 1–18, http://dx.doi.org/10.1140/epja/i2015-15167-y.
[70] T. Wilcox, T. Kawano, G.W. McKinney, J.S. Hendricks, Correlated gammas using CGM and MCNPX, Prog. Nucl. Energy 63 (2013) 1–6, http://dx.doi.org/10.1016/j.pnucene.2012.10.002, URL https://www.sciencedirect.com/science/article/pii/S0149197012001278.
[71] H. Selby, M.M. Innes, D. Barr, A. Keksis, R. Meade, C. Burns, M. Chadwick, T. Wallstrom, Fission product data measured at los alamos for fission spectrum and thermal neutrons on ^{239}Pu, ^{235}U, ^{238}U, Nucl. Data Sheets 111 (12) (2010) 2891–2922, http://dx.doi.org/10.1016/j.nds.2010.11.002, arXiv:https://doi.org/doi:10.1016/j.nds.2010.11.002, URL http://www.sciencedirect.com/science/article/pii/S0090375210001018.
[72] K.H. Schmidt, B. Jurado, C. Amouroux, C. Schmitt, General description of fission observables: GEF model code, Nucl. Data Sheets 131 (2016) 107–221, http://dx.doi.org/10.1016/j.nds.2015.12.009, arXiv:https://doi.org/10.1016/j.nds.2015.12.009.
[73] S. Nagy, K.F. Flynn, J.E. Gindler, J.W. Meadows, L.E. Glendenin, Mass distributions in monoenergetic-neutron-induced fission of ^{238}U, Phys. Rev. C 17 (1) (1978) 163–171, URL arXiv:https://doi.org/10.1103/PhysRevC.17.163.
[74] A. Sood, R. Forster, D. Kent Parsons, Analytical benchmark test set for criticality code verification, Prog. Nucl. Energy 42 (1) (2003) 55–106, http://dx.doi.org/10.1016/S0149-1970(02)00098-7, URL https://www.sciencedirect.com/science/article/pii/S0149197002000987.
[75] R.L. Martz, MCNP6 unstructured mesh initial validation and performance results, Nucl. Technol. 180 (3) (2012) 316–335, http://dx.doi.org/10.13182/NT12-A15347, arXiv:https://doi.org/10.13182/NT12-A15347.
[76] J.A. Kulesza, R.L. Martz, Evaluation of pulsed sphere time-of-flight and neutron attenuation experimental benchmarks using MCNP6's unstructured mesh capabilities, Nucl. Technol. 195 (1) (2016) 44–54, http://dx.doi.org/10.13182/NT15-121, arXiv:https://doi.org/10.13182/NT15-121.
[77] C.C. Byers, Cross sections of various materials in the godiva and jezebel critical assemblies, Nucl. Sci. Eng. 8 (6) (1960) 608–614, http://dx.doi.org/10.13182/NSE60-A25848, arXiv:https://doi.org/10.13182/NSE60-A25848.
[78] M. Chadwick, S. Frankle, H. Trellue, P. Talou, T. Kawano, P. Young, R. MacFarlane, C. Wilkerson, Evaluated iridium, yttrium, and thulium cross sections and integral validation against critical assembly and bethe sphere measurements, Nucl. Data Sheets 108 (12) (2007) 2716–2741, http://dx.doi.org/10.1016/j.nds.2007.11.005, Special Issue on Evaluations of Neutron Cross Sections. URL https://www.sciencedirect.com/science/article/pii/S0090375207000993.
[79] R. Stoller, S. Golubov, C. Domain, C. Becquart, Mean field rate theory and object kinetic Monte Carlo: A comparison of kinetic models, J. Nucl. Mater. 382 (2) (2008) 77–90, http://dx.doi.org/10.1016/j.jnucmat.2008.08.047.
[80] R.R. Wixom, A.F. Wright, Formation energies, binding energies, structure, and electronic transitions of si divacancies studied by density functional calculations, Phys. Rev. B 74 (2006) 205208, http://dx.doi.org/10.1103/PhysRevB.74.205208, URL https://link.aps.org/doi/10.1103/PhysRevB.74.205208.
[81] A.F. Wright, R.R. Wixom, Density-functional-theory calculations for silicon vacancy migration, J. Appl. Phys. 103 (8) (2008) 083517, http://dx.doi.org/10.1063/1.2906342, arXiv:https://doi.org/10.1063/1.2906342.
[82] L.J. Munro, D.J. Wales, Defect migration in crystalline silicon, Phys. Rev. B 59 (1999) 3969–3980, http://dx.doi.org/10.1103/PhysRevB.59.3969, URL https://link.aps.org/doi/10.1103/PhysRevB.59.3969.
[83] J.A. Stewart, N.A. Modine, R. Dingreville, Re-examining the silicon self-interstitial charge states and defect levels: A density functional theory and bounds analysis study, AIP Adv. 10 (9) (2020) 095004, http://dx.doi.org/10.1063/5.0016134, arXiv:https://doi.org/10.1063/5.0016134.
[84] M. Posselt, F. Gao, D. Zwicker, Migration of di- and tri-interstitials in silicon, Nucl. Instrum. Methods Phys. Res. B 228 (1) (2005) 212–217, http://dx.doi.org/10.1016/j.nimb.2004.10.046, Proceedings of the Seventh International Conference on Computer Simulation of Radiation Effects in Solids. URL https://www.sciencedirect.com/science/article/pii/S0168583X04011073.
[85] D.A. Richie, J. Kim, S.A. Barr, K.R.A. Hazzard, R. Hennig, J.W. Wilkins, Complexity of small silicon self-interstitial defects, Phys. Rev. Lett. 92 (2004) 045501, http://dx.doi.org/10.1103/PhysRevLett.92.045501, URL https://link.aps.org/doi/10.1103/PhysRevLett.92.045501.
[86] G.C. Messenger, J.P. Spratt, The effects of neutron irradiation on germanium and silicon, Proc. IRE 46 (6) (1958) 1038–1044, http://dx.doi.org/10.1109/JRPROC.1958.286841.
[87] K. Wu, J. Li, D. Zou, Y. Lu, J. Feng, X. Lv, D. Qiu, X. Fan, X. Xu, J. Wu, Neutron flux effects in silicon based bipolar junction transistors, Nucl. Instrum. Methods Phys. Res. A 913 (2019) 85–90, http://dx.doi.org/10.1016/j.nima.2018.10.037, URL https://www.sciencedirect.com/science/article/pii/S0168900218313512.
[88] G. Meneghesso, A. Paccagnella, D. Camin, N. Fedyakin, G. Pessina, C. Canali, Study of neutron damage in GaAs MESFETs, IEEE Trans. Nucl. Sci. 44 (3) (1997) 840–846, http://dx.doi.org/10.1109/23.603762.
[89] H.J. Barnaby, R.D. Schrimpf, K.F. Galloway, X. Li, J. Yang, C. Liu, Displacement damage in bipolar junction transistors: Beyond messenger-spratt, IEEE Trans. Nucl. Sci. 64 (1) (2017) 149–155, http://dx.doi.org/10.1109/TNS.2016.2615628.
[90] L. Li, J.-M. Shi, X.-Q. Liu, J.-Q. Yang, X.-W. Wang, Z.-H. Li, P. Zheng, G. Zeng, Current gain degradation model of displacement damage for drift BJTs, IEEE Trans. Nucl. Sci. 66 (4) (2019) 716–723, http://dx.doi.org/10.1109/TNS.2019.2905866.